RSC Applied Interfaces

ROYAL SOCIETY OF CHEMISTRY

PAPER

View Article Online
View Journal | View Issue

Cite this: *RSC Appl. Interfaces*, 2025, **2**, 1051

The role of Ni substitution in manganite perovskite Li–O_2 battery†

Sandra Sajeev, [a] Mewin Vincent, [a] Piotr Garbacz, [a] Marcin Strawski, [a] Chunyu Zhu, [b] Yoshitaka Aoki [c] and Damian Kowalski *[a]

A fundamental understanding of the electrochemical processes in Li–O_2 batteries is critical for the further development and commercialization of Li–O_2 and air-breathing battery technology. This study explores the electrochemistry of nickel-substituted manganite perovskites, $La_{0.7}Sr_{0.3}Mn_{1-x}Ni_xO_3$ (x = 0, 0.1, 0.3, 0.5), which were subsequently used as catalysts in Li–O_2 battery operating in 1 mol dm^{-3} bis trifluoromethane sulfonimide lithium salt (LiTFSi) in tetra ethylene glycol dimethyl ether (TEGDME) electrolyte. *In situ* Raman spectroscopy fingerprints on the discharge products correlated with charge–discharge profiles revealed that the electrochemical reaction pathway involves the formation of superoxide (LiO_2) followed by reduction to lithium peroxide (Li_2O_2) during the battery discharge and corresponding two-step oxidation process in the charge phase. The superoxide (LiO_2) was exceptionally stable for more than 2 h, which is in contrast to previous studies and expectations for short-lifetime intermediate formations. Electrochemical analysis revealed a significant improvement in the Li–O_2 battery performance for oxygen electrodes substituted with 10% of nickel, reaching a specific capacity of 3554 mAh g^{-1}. Substitution of Mn with Ni in $La_{0.7}Sr_{0.3}Mn_{0.9}Ni_{0.1}O_3$ led to enhanced charge transfer kinetics due to a high surface population of the low valence state of B-site ions (Mn^{3+}/Mn^{4+} ratio) accommodating the presence of e_g^1 electrons in line with Jahn–Teller disordered metal–oxygen octahedra effect. The current finding offers new insights for designing of aprotic LiO_2 batteries.

Received 22nd February 2025,
Accepted 19th April 2025

DOI: 10.1039/d5lf00050e

rsc.li/RSCApplInter

Introduction

Lithium–air (Li–air) and lithium–oxygen (Li–O_2) batteries have a high potential to become an efficient energy storage solution because of their relatively high theoretical energy density estimated to be 11 400 W h kg^{-1}, comparable to that of gasoline.[1,2] One of the benefits over conventional lithium-ion batteries is the advantage of utilizing oxygen from air-breathing electrode or pure oxygen, significantly reducing the battery's weight, which is beneficial for commercial applications in electric vehicles and aviation.[1–4] The electrochemical process in Li–O_2 battery is based on the reduction of molecular oxygen, O_2, on the cathode side to form lithium peroxide (Li_2O_2) upon discharge process and recovery of O_2 from the discharge product during the charging process. It is generally accepted that the main discharge product is lithium peroxide (Li_2O_2) whereas lithium superoxide (LiO_2) and lithium oxide (Li_2O) formation, stability, and their impact on battery operation is under debate. The reversibility of discharge products on the cathode side is the main bottleneck of Li–O_2 technology, hampering its commercialization. A key enabling component in the battery system is a chemically stable electrocatalyst with inartistic catalytic active sites necessary for efficient oxygen reduction and oxygen evolution reactions, which further decide the battery's power density and energy efficiency. The application of noble metals and platinum group metals, palladium (Pd),[5] silver (Ag),[6] ruthenium (Ru),[7] gold (Au),[8] and platinum (Pt)[9] catalysts has been extensively studied and is rather limited to fundamental studies due to relatively high costs.[10] Among the cost-effective materials, transition metal nitrides/oxides,[11–13] carbon-promoted transition materials,[14] conductive polymers,[15] and functional carbon metals[16] have been examined.

Perovskite-type compounds have attained recent attention because of their chemical and structural flexibility, improved oxygen mobility, high catalytic activity and reduced cost, making them promising candidates as bifunctional catalysts

[a] *Faculty of Chemistry and Biological and Chemical Research Centre, University of Warsaw, Zwirki i Wigury 101, Warsaw 02-089, Poland.*
E-mail: damian.kowalski@chem.uw.edu.pl
[b] *School of Low-carbon Energy and Power Engineering, China University of Mining and Technology, Xuzhou 221116, China*
[c] *Faculty of Engineering, Hokkaido University, Kita-Ku Kita 13, Jo Nishi 8, Sapporo 060-8628, Hokkaido, Japan*

† Electronic supplementary information (ESI) available: Charge–discharge curves, ratios of active material, carbon, and binder, analysis of XPS spectra. See DOI: https://doi.org/10.1039/d5lf00050e

in metal–air batteries.[17,18] The catalytic activity of perovskite-type compounds may be effectively controlled by the substitution of B-site ion on the corner of the perovskite lattice.[19–21] Recent reports indicate that Ni-substitution of double perovskite, $La_{1-x}Sr_xMn_{1-y}Ni_yO_3$ creates structure distortion and oxygen vacancies thus enhancing the catalytic activity of cathode in metal-air battery.[22]

The substitution of B-site ion in the lattice changes the population of oxygen vacancies in the lattice, as well as the configuration of B–O bonds and corresponding surface state, typically boosting oxygen evolution and oxygen reduction reaction performance. By fine-tuning the ratio of nickel to manganese, it is possible to enhance the electronic and structural properties of the material, leading to improved electrocatalytic performance.[19,23] $La_{1-x}Sr_xMnO_3$ has been previously studied as a prominent perovskite-type catalyst for oxygen reduction reaction (ORR).[24] The low activity towards oxygen evolution reaction (OER) is possibly associated with low covalency of the Mn–O bond and deficiency of highly active transition metal ions, thereby hindering the rechargeability and degrading the overall cell performance in the battery systems. Recent studies demonstrated that the nickel substitution played an important role in enhancing the OER catalytic activity in various catalytic systems.[19,22] In the current study, we investigate the performance of $La_{0.7}Sr_{0.3}Mn_{1-x}Ni_xO_3$ depending on the substitution level of nickel, supported by *in situ* observations on Li_2O_2, LiO_2 having fundamental aspects on Li–O_2 battery operation (Fig. 1).

Results and discussion

$La_{0.7}Sr_{0.3}Mn_1Ni_0O_3$ perovskite crystalizes in the $R\bar{3}c$ space group (no. 167) with lattice constants a = 5.50300 Å, c = 13.4241 Å and cell volume of 349.916086 Å3 (PDF 96-152-1157).[25,26] The double perovskite has a general formula of $AA'BB'O_3$ having BO_6 units constructing a three-dimensional structure of corner-sharing MnO_6 octahedra with A cations located in the interstitial spaces. The ions La^{3+}/Sr^{4+} occupying the A-site are nine-fold coordinated, while the Mn^{3+}/Mn^{4+} ions that occupy the octahedral B-site are six-fold coordinated, according to $R\bar{3}c$ symmetry (Fig. 2).XRD patterns of $La_{0.7}Sr_{0.3}Mn_{1-x}Ni_xO_3$, where x = 0, 0.1, 0.3, 0.5, are depicted in Fig. 3c. The crystallite size calculated by Scherrer equation is 16.3, 15.8, 16.9, and 17.8 nm, for $La_{0.7}Sr_{0.3}Mn_1O_3$, $La_{0.7}Sr_{0.3}Mn_{0.9}Ni_{0.1}O_3$, $La_{0.7}Sr_{0.3}Mn_{0.7}Ni_{0.3}O_3$, and $La_{0.7}Sr_{0.3}$-$Mn_{0.5}Ni_{0.5}O_3$, respectively. The splitting of characteristic peaks of $La_{0.7}Sr_{0.3}Mn_{0.5}Ni_{0.5}O_3$ shows the rhombohedral distortion of the perovskite structure.[27] The substantial peak splitting for $La_{0.7}Sr_{0.3}Mn_{0.5}Ni_{0.5}O_3$ is typically observed for all peaks except the (100) reflections. Variations from the ideal cubic form cause a small elongation or compression along the body diagonal of the unit cell. The preservation of the unsplit (100) peaks and the splitting of other reflections gives strong evidence that the distortion is rhombohedral. This structural shift is most noticeable at the highest nickel content (x = 0.5), implying a relationship between nickel doping and the degree of rhombohedral distortion.

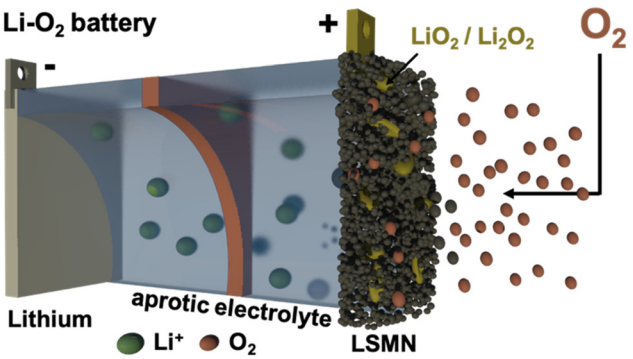

Fig. 1 Scheme of Li–O_2 battery with $La_{0.7}Sr_{0.3}Mn_{1-x}Ni_xO_3$ double perovskite catalyst (LSMN) in the cathode. Red, green and yellow spheres correspond to lithium ions, oxygen, and superoxide/peroxide compounds, respectively.

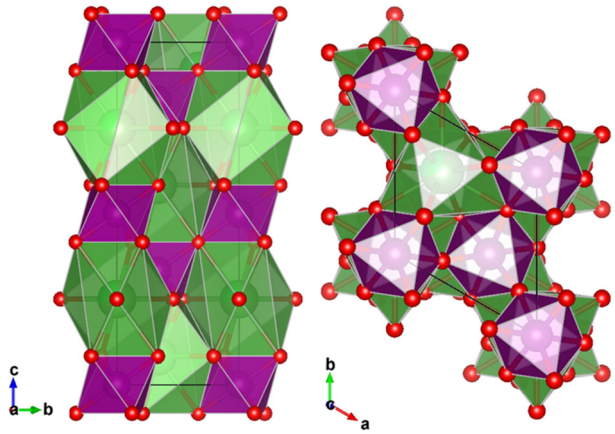

Fig. 2 Crystallographic structure of the $AA'BB'O_3$ double perovskite of $La_{0.7}Sr_{0.3}Mn_1Ni_0O_3$ compound having a 167 $R\bar{3}c$ symmetry. The unit cell dimensions are a = 5.50300 Å, b = 5.50300 Å, c = 13.4241 Å and cell volume of 349.916086 Å^3.

The *ex situ* Raman spectroscopy results for the as-formed catalysts (Fig. 3d), the peaks that have been detected convey significant details about the structural properties of double perovskites. A characteristic of perovskite-type manganites, the Mn–O stretching vibration in the MnO_6 octahedra is responsible for the high-intensity peak observed at *ca.* 660 cm^{-1}.[28] The Mn–O–Mn bending mode is most likely represented by the lower intensity peak, which is located at c.a. 531 cm^{-1}. The blue shift of these peaks, which is noticed with increased nickel content, indicates that the metal-oxygen interactions are strengthening.

The Raman peaks move towards higher wavenumbers as a result of the replacement of Mn^{3+} ions by Ni^{2+} ions, which also causes a contraction of the lattice and greater metal–oxygen interactions. The observed alterations in peak locations and intensities in response to different nickel contents suggest that nickel incorporation alters the local structure and bonding environment inside the perovskite lattice, which could have an impact on the materials catalytic

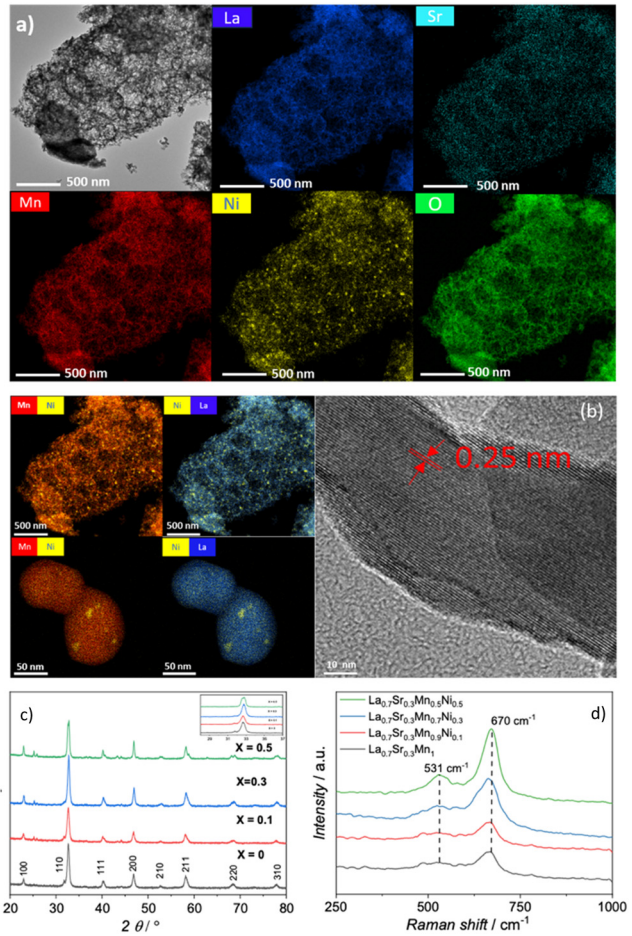

Fig. 3 TEM and corresponding EDS elemental mapping for La, Sr, Mn Ni, O and superimposed MnNi and NiLa (a and b), (c) *ex situ* XRD patterns and (d) *ex situ* Raman spectra of $La_{0.7}Sr_{0.3}Mn_{1-x}Ni_xO_3$ (x = 0, 0.1, 0.3, 0.5) pristine catalyst.

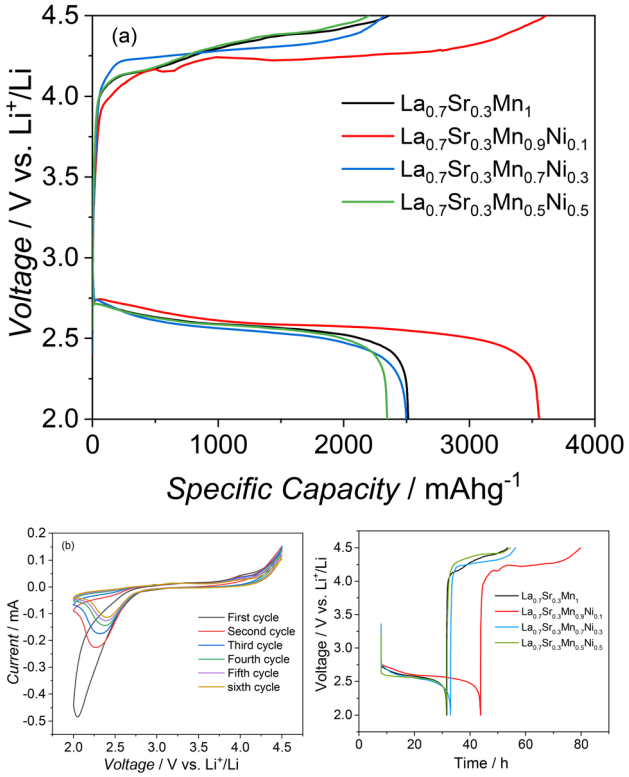

Fig. 4 a) Galvanostatic discharge and charge cycles for $La_{0.7}Sr_{0.3}Mn_1Ni_0O_3$, $La_{0.7}Sr_{0.3}Mn_{0.9}Ni_{0.1}O_3$, $La_{0.7}Sr_{0.3}Mn_{0.7}Ni_{0.3}$ O_3, and $La_{0.7}Sr_{0.3}Mn_{0.5}Ni_{0.5}O_3$ and corresponding voltage-time curves obtained at first cycle at a current density of 100 mAg^{-1} b) cyclic voltammograms of first five consecutive cycles of $La_{0.7}Sr_{0.3}Mn_{0.9}Ni_{0.1}$ at a scan rate of 0.1 mV s^{-1} in 1 mol dm^{-3} bis trifluoromethane sulfonimide lithium salt (LiTFSi) in tetra ethylene glycol dimethyl ether (TEGDME).

characteristics. TEM (HAADF) images with corresponding high-resolution EDS elemental maps in Fig. 3a and b show the homogeneous distribution of La, Sr, Mn and O in $La_{0.7}Sr_{0.3}Mn_{0.5}Ni_{0.5}O_3$ structure.

The superimposed EDS elemental maps for MnNi and LaNi reveal nanoregions with enriched nickel content. Those slight compositional alternations most likely contribute to the rhombohedral distortion in the double perovskite. The discharge and charge voltage profiles of cells with $La_{0.7}Sr_{0.3}Mn_{0.5}Ni_{0.5}O_3$ cathode having different ratios of active material, carbon, and binder are demonstrated in Fig. S1.† The 5 : 4 : 1 ratio most likely gives a more ideal ionic conductivity and balanced environment for ionic transport, hence increasing initial discharge capacity. Conversely, imbalances were observed in the 2 : 7 : 1 and 7 : 2 : 1 ratios resulting in higher resistance and less effective ion transport.

Hence for all the following electrochemical studies the electrode ratio of 5 : 4 : 1 was used. Fig. 4a depicts the discharge/charge voltage profiles obtained with four distinct perovskites at a discharge current density of 100 mAg^{-1}.

The cell with $La_{0.7}Sr_{0.3}Mn_1O_3$, $La_{0.7}Sr_{0.3}Mn_{0.9}Ni_{0.1}O_3$, $La_{0.7}Sr_{0.3}Mn_{0.7}Ni_{0.3}O_3$, and $La_{0.7}Sr_{0.3}$ $Mn_{0.5}Ni_{0.5}O_3$ catalysts at the cathode delivered a total discharge capacity of 2500 mAh $g^{-1}_{(electrode)}$, 3554 mAh $g^{-1}_{(electrode)}$, 2507 mAh $g^{-1}_{(electrode)}$ and 2373 mAh $g^{-1}_{(electrode)}$, respectively. Furthermore, the charge voltage plateau of $La_{0.7}Sr_{0.3}Mn_{0.9}Ni_{0.1}O_3$ is approximately 100 mV lower than $La_{0.7}Sr_{0.3}Mn_1O_3$. $La_{0.7}Sr_{0.3}Mn_{0.9}Ni_{0.1}O_3$ has better electrochemical performance and a lower discharge–charge voltage gap than other three studied electrocatalysts.

The substitution of 10% manganese with nickel is supposed to create catalytic centers oxygen reduction/oxidation reactions. The cyclic voltammetry (Fig. 4b) results for $La_{0.7}Sr_{0.3}Mn_{0.9}Ni_{0.1}O_3$ show a major decrease in peak current after the first cycle. Despite the initial fading, the CV curves general shape and structural patterns are stable across all the cycles indicating that the fundamental electrochemical process remains constant across the cycles.

A more fundamental understanding of electrochemical processes during discharge/charge was investigated using *in situ* Raman spectroscopy in Fig. 5.[29–32] Raman bands at open circuit voltage originate from the electrode, electrolyte, and optical window. In the first stage of discharge (2.41 V), two peaks appear at 1127 cm^{-1} and 1517 cm^{-1}. The O–O stretching of lithium superoxide (LiO_2) in the discharge

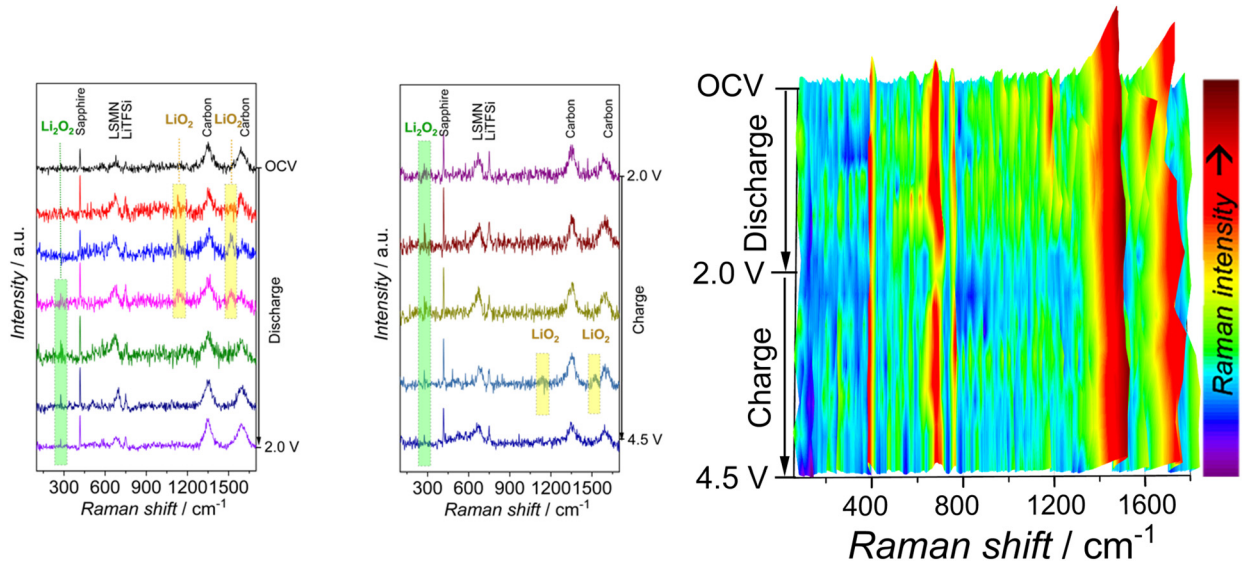

Fig. 5 *In situ* Raman spectroscopy for Li–O_2 battery composed $La_{0.7}Sr_{0.3}Mn_{0.9}Ni_{0.1}O_3$ catalyst obtained at the first discharge, charge cycle at a current density of 100 mAg^{-1} in 1 mol dm^{-3} bis trifluoromethane sulfonimide lithium salt (LiTFSi) in tetra ethylene glycol dimethyl ether (TEGDME).

products is assigned the Raman shift at 1127 cm^{-1}. The 1517 cm^{-1} Raman band is generated in conjunction with the 1127 cm^{-1} band, assigned to the LiO_2-C mode, where carbon is used as a conductive additive in the electrode.[33]

The formation and disappearance of LiO_2 is displayed in 3D *in situ* Raman spectrum in Fig. 5. The reversible processes in non-aqueous Li–O_2 cell include the development and evolution of mostly lithium peroxide (Li_2O_2) products, where superoxide (LiO_2) plays an essential role. Reference Li_2O_2 powder Sigma Aldrich gives *ex situ* Raman spectra with expected O–O stretching frequency of peroxide at around 802 cm^{-1} and Li–O vibrations located at 256 cm^{-1}.[34,35] The Li_2O_2 peak assigned to Li–O vibrations is detected at 279 cm^{-1} (Fig. 5), while the O–O stretching at 790 cm^{-1} is absent in the spectra in the current study.

Most of the studies report difficulties in peroxide detection with low intensity and broad peaks, particularly without surface enhancement.[36] The variations in the strength of the signals between the literature data[37] and the current study may arise from differences in Raman scattering from peroxide due to surface enhancement issues. Peroxide may be in the form of amorphous, crystalline or a mixture of overlapping amorphous/crystalline layers with complex morphology features. The amorphous Li_2O_2 is less coordinated than crystalline Li_2O_2, with a larger population of lithium vacancies and hole polaron defects.[38] In addition, the O–O peroxide bond is expected to be shorter for the amorphous phase. Recent studies by others indicate the presence of amorphous Li_2O_2 as a discharge product, giving unique Raman spectroscopy profiles such as higher O–O vibrational frequencies than crystalline Li_2O_2.[39–41]

In situ Raman spectra obtained during the discharge process suggest that the reduction reaction involves one electron transfer to form superoxide (O_2^-, LiO_2) in the first stage of the discharge process:

$$O_2 + e^- \rightarrow O_2^- \quad (1)$$

$$O_2^- + Li^+ \rightarrow LiO_2 \quad (2)$$

The lithium superoxide (LiO_2) is detected at first stage of discharge and further reduced to lithium superoxide (Li_2O_2) as the discharge proceeds. Lithium superoxide formation may proceed *via* i) catalyst surface route (3), and/or ii) solution-mediated route, *i.e.* disproportionation (4):[42]

$$LiO_2 + Li^+ + e^- \rightarrow Li_2O_2 \quad (3)$$

$$2LiO_2 \rightarrow Li_2O_2 + O_2 \quad (4)$$

The presence of lithium peroxide in the charge phase suggests that Li_2O_2 remains stable during the charging process. The recovery of molecular oxygen (5–6) in the charge cycle seems to proceed through a two-step oxidation process[43] involving lithium superoxide (LiO_2) formation as the O–O stretching at 1127 cm^{-1} is detected. The presence Li_2O_2 through the charge cycle indicates that the kinetics of Li_2O_2/LiO_2 oxidation is sluggish and the decomposition seems to be dominant at the end of the charge cycle.

$$Li_2O_2 \rightarrow LiO_2 + Li^+ + e^- \quad (5)$$

$$LiO_2 \rightarrow Li^+ + O_2 + e^- \quad (6)$$

Lithium superoxide (LiO_2) feature at 1127 cm^{-1} drops intensity during the charge cycle, suggesting that it is extracted from the electrode surface. It is evident from the data that LiO_2 is not merely an intermediate but rather a reversible product that forms and changes during the cycle. The main concern referring to superoxide generation is the widespread perception that superoxides are extremely

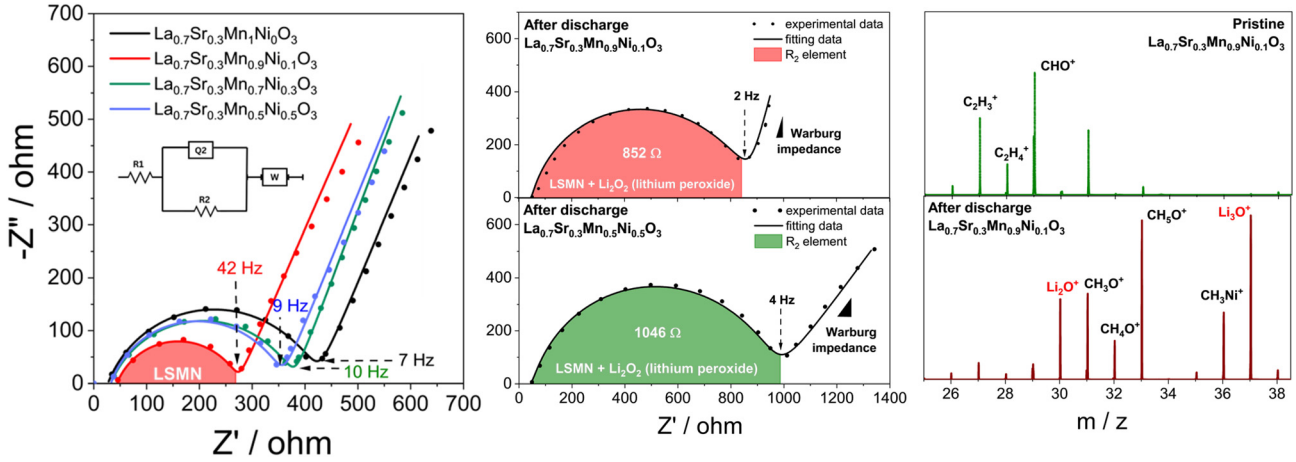

Fig. 6 *Ex situ* impedance and ToF-SIMS analysis. Electrochemical impedance spectra (EIS) for Li–O_2 battery composed of $La_{0.7}Sr_{0.3}Mn_1Ni_0O_3$, $La_{0.7}Sr_{0.3}Mn_{0.9}Ni_{0.1}O_3$, $La_{0.7}Sr_{0.3}Mn_{0.7}Ni_{0.3}O_3$, and $La_{0.7}Sr_{0.3}Mn_{0.5}Ni_{0.5}O_3$ catalyst were obtained at open circuit voltage for prisine electrode. EIS obtained after full discharge of Li–O_2 battery composed of $La_{0.7}Sr_{0.5}Mn_{0.5}Ni_{0.5}O_3$ and $La_{0.7}Sr_{0.3}Mn_{0.9}Ni_{0.1}O_3$ catalyst are shown for comparition, experimental data were fitted with an equivalent circuit of $R_1[R_2Q_2]W$. ToF-SIMS spectra were obtained of pristine (green) and fully discharged electrode (red) of $La_{0.7}Sr_{0.3}Mn_{0.9}Ni_{0.1}O_3$.

unstable. The dissolved superoxides have been proven to be kinetically stable in specific organic solvents. Recent reports by Gittleson *et al.* on superoxide stability in high-purity Li–O_2 electrolyte solvents, such as monoglyme, diglyme, tetraglyme and indicate that superoxide ions may be stable for up to 16 days.[34] In the current study the superoxide (LiO_2) is stable for two hours during the discharge process indicating its long lifetime. The potential factor influencing the stability of superoxide is the structure of the electrolyte. TEGDME has a donor number of 16.6, which comparatively promotes weak solvation of Li^+ ions compared to the solvents with high donor numbers. Due to the moderate solvation effect, the dissolution of LiO_2 in the electrolyte is typically limited, promoting the retention of LiO_2 on the electrode surface. According to the studies by Johnson *et al.*,[44] solvents having a high donor number are expected to facilitate the dissolution of LiO_2 into the electrolyte, which leads to rapid disproportionation into Li_2O_2. At the same time, solvents with low donor numbers (*e.g.*, TEGDME) tend to retain LiO_2 for a longer time on the electrode surface further proceeding to the formation of Li_2O_2 film on the electrode through disproportionation or a second electron reduction. Another critical factor is the structure of the formed lithium superoxide. The computational studies by Das *et al.*[45] suggest that the stability of lithium superoxide is related to the type and shape of the superoxide cluster formed on the electrode surface. Although LiO_2 is thermodynamically unstable according to disproportionation ($2LiO_2 \rightarrow Li_2O_2 + O_2$), in terms of kinetics, it is expected to be stable due to the reaction barrier for the O_2 removal. For example, the LiO_2 clusters have a disproportionation barrier of c.a. 1 eV, which is higher than that for LiO_2 dimer (c.a. 0.5 eV). The above scenario demonstrates that disproportionation proceeding through superoxide cluster formation, may influence its integration into the discharge product. The contact between electrolyte and LiO_2 should bring obstacles in O_2 desorption by increasing the barrier and thereby the lifetime of LiO_2.[45] Fig. 6c depicts the positive-ion TOF-SIMS spectra performed for the pristine and post-cycling electrodes. The results from the post-cycling electrode clearly show Li_2O^+ at 30.03 *m*/*z* and Li_3O^+ at 37.04 *m*/*z* secondary ions related to the fragments of lithium oxides.[3] Interpretation of higher mass peaks is rather problematic due to overlapping with organic fragments from electrolyte and binder. Lower/higher *m*/*z* peaks consist of organic compounds, and they arise from the electrolyte species. *In situ* Raman spectroscopy results combined with TOF-SIMS analysis provide strong evidence for the formation of lithium oxides.

Electrochemical impedance spectroscopy was utilized to investigate the electrocatalyst's impedance both at open circuit voltage and after discharge process. Fig. 6a and b depicts the Nyquist plots for experimental data as well as simulated data using the equivalent circuit fitting, where R_1 denotes the internal resistance of the battery; R_2 is the charge transfer resistance, representing the kinetics of an electrochemical process; Q_2 is the constant-phase element representing capacitive nature of the process or battery component; W denotes the Warburg impedance.[46–49] The simulated data matches well the experimental data across the full range of frequency with $\chi^2/|Z|^2$ fitting at 0.1. The arc located in the high-frequency zone corresponds to R_2, with the diameter depending on type of catalyst; here the reduced diameter of the arc indicates facilitated charge transfer. In the analogous circuit diagram, the straight line located in the low-frequency region represents the diffusion component, *i.e.*, Warburg impedance. The catalyst composed of $La_{0.7}Sr_{0.3}Mn_{0.9}Ni_{0.1}O_3$ possesses lowest charge transfer resistance of 273 Ω compared to 422, 377 and 356 Ω for $La_{0.7}Sr_{0.3}Mn_1O_3$, $La_{0.7}Sr_{0.3}Mn_{0.7}Ni_{0.3}O_3$ and $La_{0.7}Sr_{0.3}Mn_{0.5}Ni_{0.5}O_3$, respectively. Hence, the $La_{0.7}Sr_{0.3}Mn_{0.9}Ni_{0.1}O_3$ electrocatalyst facilitates faster electron transfer during the electrochemical reactions in the current battery configuration. The Mn^{3+}/Mn^{4+} ratio

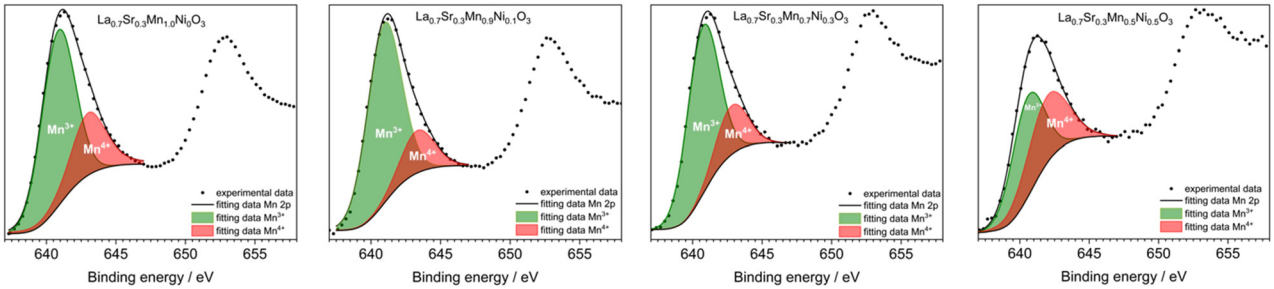

Fig. 7 Mn 2p XPS spectra for pristine $La_{0.7}Sr_{0.3}Mn_1Ni_0O_3$, $La_{0.7}Sr_{0.3}Mn_{0.9}Ni_{0.1}O_3$, $La_{0.7}Sr_{0.3}Mn_{0.7}Ni_{0.3}O_3$, and $La_{0.7}Sr_{0.3}Mn_{0.5}Ni_{0.5}O_3$ catalyst demonstrating population of Mn^{3+} on the oxide surface depending on the Ni substitution ratio. The molar ratios of Mn^{3+}/Mn^{4+} determined from fitting analysis are listed in ESI.†

seems to play a critical role in the electrical conductivity of perovskite electrodes. The connection between the Mn^{3+}/Mn^{4+} ratio and the charge storage capability is discussed further in XPS analysis.

The trend is the same in the spectra after discharge, with an evident increase in the charge transfer resistance by a factor of two. The formation of low conductivity discharge products, *i.e.* LiO_2 and Li_2O_2 on the electrode surface as indicated by *in situ* Raman supported by ToF-SIMS analysis is the main reason for a significant increase of charge transfer resistance at completed discharge. The low value of charge transfer resistance of $La_{0.7}Sr_{0.3}Mn_{0.9}Ni_{0.1}O_3$ correlates with the increased discharge–charge performance.

From the electrochemical data it is evident that 10% of nickel substitution has a beneficial impact on the catalytic activity of catalyst. The Mn and Ni valence states in $La_{0.7}Sr_{0.3}Mn_{1-x}Ni_xO_3$ are shown in XPS spectra (Fig. 7 and S2,† respectively). The Ni 3p, does not show a clear peak for $x = 0.1$ due to relatively low Ni content. Two peaks at 66.0 and 67.5 eV appear for $x = 0.3$ and $x = 0.5$ assigned to $3p_{3/2}$ and $3p_{1/2}$ spin–orbit components of Ni^{2+} states, respectively.[50,51] The $3p_{3/2}$ and $3p_{1/2}$ peaks of Ni^{3+} states of reference $LaNiO_3$ appear around 69 and 71 eV,[50] which differs from our study indicating that the Ni cations favor remaining in the Ni^{2+} valence state and the higher valence state Ni^{3+} is very scarce in all the studied double perovskites. Mn 2p spectra show variable Mn valence states with variation of x. All compositions show a sharp peak around 641 eV and a broad peak around 658 eV, attributed to $2p_{3/2}$ and $2p_{1/2}$ spin–orbit components, respectively (Fig. 7). The deconvolution of the $2p_{3/2}$ peak was performed with binding energy full width at half maximum (FWHM) kept constant. The presence of Mn^{3+} and Mn^{4+} valence states in $La_{0.7}Sr_{0.3}Mn_{1-x}Ni_xO_3$ was evident at 641.8 and 643.2 eV, respectively.[22,52] The molar ratio of Mn^{3+}/Mn^{4+} increases with increasing x from 0 to 0.1 and decreases with increasing x above 0.1 (Table S4†) indicating the highest population of Mn^{3+} oxidation states in $La_{0.7}Sr_{0.3}Mn_{0.9}Ni_{0.1}O_3$, in which more than 90% of the manganese ions occupy the Mn^{3+} valence state.

The catalytic centers for oxygen reduction reaction tend to be associated with a high population of lower valence states of manganese ions. One of the most efficient catalysts reported for oxygen reduction reaction are cobalt oxides containing Co^{3+} ions in the intermediate spin state $t_{2g}^5e_g^1$.[53] The manganese oxides containing Mn^{3+}, which are at the highest population on the surface of $La_{0.7}Sr_{0.3}Mn_{0.9}Ni_{0.1}O_3$ catalyst are in the $t_{2g}^3e_g^1$ spin state. The similarity between both transition metals is that they have Jahn-Teller disordered metal–oxygen octahedra due to the presence of e_g^1 electrons.[53] Several studies indicated that the presence of e_g^1 electrons of redox-active transition metal atoms, *i.e.*, B-site cations has a key impact on the catalytic activity of the perovsites.[19,53] The presence of a single e_g^1 electron is expected to improve the electronic communication in the oxide structure[54] and, therefore facilitate the charge transfer kinetics as observed for catalysts composed of $La_{0.7}Sr_{0.3}Mn_{1-x}Ni_xO_3$ at the maximum population of Mn^{3+} states.

Conclusions

Nickel-substituted lanthanum strontium manganite $La_{0.7}Sr_{0.3}Mn_{1-x}Ni_xO_3$ perovskite with x level of 0, 0.1, 0.3, and 0.5 was synthesized using citrate precursor method and studied as an oxygen electrode in an aprotic Li–O_2 battery operating in 1 mol dm^{-3} bis trifluoromethane sulfonimide lithium salt (LiTFSi) in tetra ethylene glycol dimethyl ether (TEGDME) electrolyte. The substitution of manganese with nickel was optimized to achieve high electrocatalytic activity of oxygen electrode; at a current density of 100 mAg^{-1} in a voltage window of 2.0–4.5 V *vs.* Li^+/Li, the discharge capacity for $La_{0.7}Sr_{0.3}Mn_{0.9}$ $Ni_{0.1}O_3$ catalyst was 3554 mAh g^{-1}. The *in situ* Raman spectroscopy revealed lithium superoxide (LiO_2) formation during discharge and its further reduction to lithium peroxide (Li_2O_2). A reversible formation of LiO_2 from Li_2O_2 was observed during the charge stage. The superoxide (LiO_2) was electrochemically stable for the first two hours at the discharge, indicating that LiO_2 is more stable than expected for short-lifetime intermediates such as superoxides. The formation of stable and reversible LiO_2 is in contrast to earlier reports proposed that LiO_2 is an intermediate in the formation of Li_2O_2.

Experimental section

Materials synthesis. The citrate precursor method was employed to prepare specimens of $La_{0.7}Sr_{0.3}Mn_{1-x}Ni_xO_3$ (x = 0, 0.1, 0.3, 0.5). La $(NO_3)_3{\cdot}6H_2O$ (Sigma-Aldrich, ≥99.99%), Sr $(NO_3)_2$ (Sigma-Aldrich, ≥99.99%), Mn $(NO_3)_2{\cdot}6H_2O$ (Sigma-

Aldrich, ≥99.99%), and Ni $(NO_3)_2{\cdot}6H_2O$ (Sigma-Aldrich, ≥99.99%) were the primary reagents used for the synthesis. Following the proper dissolution of the reagents in distilled water, an equal molar ratio of citric acid (Sigma-Aldrich, ≥99.5%) was added as a complex agent. The citrate solution was heated to 64 °C while being agitated to promote polymerization. After being prefired in air for one hour at 450 °C, the resultant product was fired for twelve hours at 800 °C in an O_2 environment. The morphological aspects for of $La_{0{\cdot}7}Sr_{0{\cdot}3}Mn_{1-x}Ni_xO_3$ have been discussed elsewhere.[19]

Materials characterization. XRD analysis was performed with Rigaku Rint-2000 using Cu Kα radiation (wavelength 1.5405). The Debye–Scherrer equation ($D = K\lambda/\beta\cos\theta$) was used to calculate the average crystallite size of the catalyst. K is an arbitrary constant having a value of 0.9, the wavelength of the source radiation is λ, the full width at half maximum (FWHM) of the most significant peak in the XRD spectrum is represented by β, and θ is the angle of diffraction. A transmission electron microscope (FEI, Talos F200X) provided with tools for an energy-dispersive X-ray spectroscope (Bruker Super-X EDS system) was used to observe specimens morphology. Raman scattering spectra were collected using a DXR3 Raman Microscope (Thermo Scientific) equipped with a 50× objective having a numerical aperture of 0.25, a spot size of 2.88 μm, and a DPSS laser (532 nm). To ensure the alignment of spectra, the cell was calibrated prior to the experiment. In order to prevent sample deterioration and unintended side reactions, the laser power was kept at 1% maximum intensity.

Electrochemical techniques. The composite electrode was prepared by mixing 50 wt% of active material, 40 wt% acetylene black, and 10 wt% polyvinylidene fluoride (PVDF). All the components were added and mixed with *N*-methyl-2-pyrrolidone (NMP) to form a slurry of uniform consistency. The resultant mixture was uniformly distributed in small circular pieces of nickel mesh and dried overnight at 90 °C in a muffle furnace under an oxygen atmosphere to completely remove the solvent from the electrode surface.

The assembly of ECC-Air electrochemical cells (EL-CELL) was done inside an argon-filled glove box (mBraun Labstar) with the moisture and oxygen levels kept <0.5 ppm. The Li–O_2 cells were assembled with a lithium metal anode, a glass fiber separator (GF/B, Whatman), and an electrolyte composed of 1 mol dm^{-3} LiTFSi (Bis(trifluoromethane) sulfonimide lithium salt, ≥99.0%) in TEGDME (tetra ethylene glycol dimethyl ether), and $La_{0.7}Sr_{0.3}Mn_{1-x}Ni_xO_3$ catalyst cathode.

The electrochemical performance of the batteries was tested using BioLogic SP-300 potentiostat. Before applying electrochemical protocol, rest time was given for all the cells for 8 hours with O_2 flow. For the study of the discharge/charge cycles a constant current of 100 mAg^{-1} was applied in 2.0–4.5 V *vs.* Li^+/Li voltage window. The specific capacities were calculated by normalizing the mass of the catalyst loaded at the cathode. The cyclic voltammetry was performed with a scan rate of 0.1 mV s^{-1}. The electrochemical impedance spectroscopy (EIS) study was performed at open-circuit potential before and after discharge in the frequency range 10^5 to 10^{-1} Hz, using a sinusoidal voltage signal amplitude of 5 mV. The impedance spectra were analyzed using an equivalent circuit model $R_1[R_2Q_2]W$. The experimental data were fitted to the corresponding circuit using BioLogic's EC-Lab software. The distribution of ions over the sample surface was obtained with a time-of-flight secondary ion mass spectrometry (TOF-SIMS). The measurements were performed on a TOF-SIMS.5 spectrometer (ION-TOF GmbH, Germany) operating in Bi^{3+} mode (at 30 keV energy and 0.48 pA ion current conditions). The LSMN powder was pressed onto copper tape to form a thick layer as a reference sample. The electrode grid after discharge was mounted gently using metal clips. The base pressure in the chamber was below 2×10^{-9} mbar. Analyses were done over 500 μm × 500 μm area. The internal mass calibration was performed using mass a series of ions: Li^+, Na^+, K^+, Mn^+, La^+. Identification of molecular ions and fragments was performed using SurfaceLab 7.0 software (ION-TOF GmbH, Germany).

Data availability

The data supporting this article have been included as part of the ESI.†

Author contributions

Sandra Sajeev: investigation, methodology, writing – original draft. Mewin Vincent: methodology. Marcin Stawski: methodology, analysis. Piotr Garbacz: resources. Chunyu Zhu: resources. Yoshitaka Aoki: methodology, resources, Damian Kowalski: supervision, manuscript writing.

Conflicts of interest

There are no conflicts to declare.

Acknowledgements

The current study was financially supported by National Science Centre (OPUS20) grant number 2020/39/B/ST4/02548. The authors would like to thank K. Sobczak for TEM measurements and Szymon Sutula for XRD analysis.

Notes and references

1 W.-J. Kwak, Rosy, D. Sharon, C. Xia, H. Kim, L. R. Johnson, P. G. Bruce, L. F. Nazar, Y.-K. Sun, A. A. Frimer, M. Noked, S. A. Freunberger and D. Aurbach, *Chem. Rev.*, 2020, **120**, 6626–6683.
2 P. G. Bruce, S. A. Freunberger, L. J. Hardwick and J.-M. Tarascon, *Nat. Mater.*, 2012, **11**, 19–29.
3 H.-G. Jung, J. Hassoun, J.-B. Park, Y.-K. Sun and B. Scrosati, *Nat. Chem.*, 2012, **4**, 579–585.
4 A. Kondori, M. Esmaeilirad, A. M. Harzandi, R. Amine, M. T. Saray, L. Yu, T. Liu, J. Wen, N. Shan, H.-H. Wang, A. T. Ngo, P. C. Redfern, C. S. Johnson, K. Amine, R. Shahbazian-Yassar, L. A. Curtiss and M. Asadi, *Science*, 2023, **379**, 499–505.

5 Z. Cui, L. Li, A. Manthiram and J. B. Goodenough, *J. Am. Chem. Soc.*, 2015, **137**, 7278–7281.
6 Q. Hong and H. Lu, *Sci. Rep.*, 2017, **7**, 3378.
7 B. Sun, P. Munroe and G. Wang, *Sci. Rep.*, 2013, **3**, 2247.
8 Y.-C. Lu, D. G. Kwabi, K. P. C. Yao, J. R. Harding, J. Zhou, L. Zuin and Y. Shao-Horn, *Energy Environ. Sci.*, 2011, **4**, 2999–3007.
9 G. Zhao, J. Lv, Z. Xu, L. Zhang and K. Sun, *J. Power Sources*, 2014, **248**, 1270–1274.
10 J. Zhao, R. Pathak, Z. Zhao, X. Chen, M. B. Saud, H. Li, F. Wu, Q. Qiao, J. W. Elam and X. Wang, *Green Chem.*, 2023, **25**, 10182–10208.
11 F. Li, R. Ohnishi, Y. Yamada, J. Kubota, K. Domen, A. Yamada and H. Zhou, *Chem. Commun.*, 2013, **49**, 1175–1177.
12 A. Débart, A. J. Paterson, J. Bao and P. G. Bruce, *Angew. Chem., Int. Ed.*, 2008, **47**, 4521–4524.
13 S. H. Oh, R. Black, E. Pomerantseva, J.-H. Lee and L. F. Nazar, *Nat. Chem.*, 2012, **4**, 1004–1010.
14 J.-L. Shui, N. K. Karan, M. Balasubramanian, S.-Y. Li and D.-J. Liu, *J. Am. Chem. Soc.*, 2012, **134**, 16654–16661.
15 Y. Cui, Z. Wen, X. Liang, Y. Lu, J. Jin, M. Wu and X. Wu, *Energy Environ. Sci.*, 2012, **5**, 7893–7897.
16 S. Wang, S. Dong, J. Wang, L. Zhang, P. Han, C. Zhang, X. Wang, K. Zhang, Z. Lan and G. Cui, *J. Mater. Chem.*, 2012, **22**, 21051–21056.
17 G. Liu, H. Chen, L. Xia, S. Wang, L.-X. Ding, D. Li, K. Xiao, S. Dai and H. Wang, *ACS Appl. Mater. Interfaces*, 2015, **7**, 22478–22486.
18 D. U. Lee, H. W. Park, M. G. Park, V. Ismayilov and Z. Chen, *ACS Appl. Mater. Interfaces*, 2015, **7**, 902–910.
19 Y. Aoki, E. Tsuji, T. Motohashi, D. Kowalski and H. Habazaki, *J. Phys. Chem. C*, 2018, **122**, 22301–22308.
20 D. Kowalski, H. Kiuchi, T. Motohashi, Y. Aoki and H. Habazaki, *ACS Appl. Mater. Interfaces*, 2019, **11**, 28823–28829.
21 E. Tsuji, T. Motohashi, H. Noda, D. Kowalski, Y. Aoki, H. Tanida, J. Niikura, Y. Koyama, M. Mori, H. Arai, T. Ioroi, N. Fujiwara, Y. Uchimoto, Z. Ogumi and H. Habazaki, *ChemSusChem*, 2017, **10**, 2864–2868.
22 Z. Wang, Y. You, J. Yuan, Y.-X. Yin, Y.-T. Li, S. Xin and D. Zhang, *ACS Appl. Mater. Interfaces*, 2016, **8**, 6520–6528.
23 Y. Aoki, K. Takase, H. Kiuchi, D. Kowalski, Y. Sato, H. Toriumi, S. Kitano and H. Habazaki, *J. Am. Chem. Soc.*, 2021, **143**, 6505–6515.
24 W. Wang, W. Liu, M. Kamiko and S. Yagi, *New J. Chem.*, 2022, **46**, 13082–13088.
25 M. C. Ramírez Camacho, C. F. Sánchez Valdés, M. Curiel, J. L. Sánchez Llamazares, J. M. Siqueiros and O. Raymond Herrera, *Sci. Rep.*, 2020, **10**, 2568.
26 H.-S. Lee and H.-H. Park, *Adv. Condens. Matter Phys.*, 2015, **2015**, 746475.
27 T. I. M. Vaz, S. M. Gurav and A. V. Salker, *Indones. J. Chem.*, 2021, **21**, 1244–1251.
28 N. Bajpai, M. Saleem and A. Mishra, *J. Mater. Sci.: Mater. Electron.*, 2021, **32**, 12890–12902.
29 M. Vincent and D. Kowalski, *ACS Appl. Nano Mater.*, 2023, **6**, 6528–6537.
30 M. Vincent, S. Sajeev, M. Srivastava, E. Kowalska, S. Srinivasan and D. Kowalski, *Electrochim. Acta*, 2025, **509**, 145309.
31 L. Fadillah, D. Kowalski, M. Vincent, C. Zhu, S. Kitano, Y. Aoki and H. Habazaki, *ACS Appl. Mater. Interfaces*, 2023, **15**, 52563–52570.
32 M. Vincent, S. S. Kumar and D. Kowalski, *Electrochim. Acta*, 2023, **469**, 143161.
33 A. Halder, H.-H. Wang, K. C. Lau, R. S. Assary, J. Lu, S. Vajda, K. Amine and L. A. Curtiss, *ACS Energy Lett.*, 2018, **3**, 1105–1109.
34 F. S. Gittleson, W.-H. Ryu and A. D. Taylor, *ACS Appl. Mater. Interfaces*, 2014, **6**, 19017–19025.
35 J. Yang, D. Zhai, H.-H. Wang, K. C. Lau, J. A. Schlueter, P. Du, D. J. Myers, Y.-K. Sun, L. A. Curtiss and K. Amine, *Phys. Chem. Chem. Phys.*, 2013, **15**, 3764–3771.
36 T. A. Galloway and L. J. Hardwick, *J. Phys. Chem. Lett.*, 2016, **7**, 2119–2124.
37 S. Higashi, Y. Kato, K. Takechi, H. Nakamoto, F. Mizuno, H. Nishikoori, H. Iba and T. Asaoka, *J. Power Sources*, 2013, **240**, 14–17.
38 F. Tian, M. D. Radin and D. J. Siegel, *Chem. Mater.*, 2014, **26**, 2952–2959.
39 Y. Wang, S. Pan, H. Li, D. Li, Y. Guo, S. Chi, C. Geng, S. Wu and Q.-H. Yang, *EES Catal.*, 2023, **1**, 312–321.
40 Y. Dou, X.-G. Wang, D. Wang, Q. Zhang, C. Wang, G. Chen, Y. Wei and Z. Zhou, *Chem. Eng. J.*, 2021, **409**, 128145.
41 F. S. Gittleson, K. P. C. Yao, D. G. Kwabi, S. Y. Sayed, W.-H. Ryu, Y. Shao-Horn and A. D. Taylor, *ChemElectroChem*, 2015, **2**, 1446–1457.
42 M. Aoki, D. Dilixiati, M. Ushijima, S. Yamada and T. Kondo, *J. Phys. Chem. C*, 2023, **127**, 15051–15061.
43 B. M. Gallant, D. G. Kwabi, R. R. Mitchell, J. Zhou, C. V. Thompson and Y. Shao-Horn, *Energy Environ. Sci.*, 2013, **6**, 2518–2528.
44 L. Johnson, C. Li, Z. Liu, Y. Chen, S. A. Freunberger, P. C. Ashok, B. B. Praveen, K. Dholakia, J.-M. Tarascon and P. G. Bruce, *Nat. Chem.*, 2014, **6**, 1091–1099.
45 U. Das, K. C. Lau, P. C. Redfern and L. A. Curtiss, *J. Phys. Chem. Lett.*, 2014, **5**, 813–819.
46 T. L. Kulova, V. A. Tarnopol'skii and A. M. Skundin, *Russ. J. Electrochem.*, 2009, **45**, 38–44.
47 M. Gaberšček, *Curr. Opin. Electrochem.*, 2022, **32**, 100917.
48 M. Gaberšček, *Nat. Commun.*, 2021, **12**, 6513.
49 B. A. Boukamp, *Solid State Ionics*, 1986, **20**, 31–44.
50 J. G. Kim, D. L. Pugmire, D. Battaglia and M. A. Langell, *Appl. Surf. Sci.*, 2000, **165**, 70–84.
51 M. Saghayezhian, Z. Wang, H. Guo, Y. Zhu, E. W. Plummer and J. Zhang, *Phys. Rev. B*, 2017, **95**, 165434.
52 J. Hu, L. Wang, L. Shi and H. Huang, *Electrochim. Acta*, 2015, **161**, 115–123.
53 U. Maitra, B. S. Naidu, A. Govindaraj and C. N. R. Rao, *Proc. Natl. Acad. Sci. U. S. A.*, 2013, **110**, 11704–11707.
54 H. Yadegari, M. Norouzi Banis, A. Lushington, Q. Sun, R. Li, T.-K. Sham and X. Sun, *Energy Environ. Sci.*, 2017, **10**, 286–295.